Chapter 2

Low Melting Temperature Solder Materials for Use in Flexible Microelectronic Packaging Applications

Sang Hoon Kim and Sangsun Yang

Additional information is available at the end of the chapter

http://dx.doi.org/10.5772/intechopen.70272

Abstract

The increasing application of heat-sensitive microelectronic components such as a multitude of transistors, polymer-based microchips, and so on, and flexible polymer substrates including polyethylene terephthalate (PET) and polyimide (PI), among others, for use in wearable devices has led to the development of more advanced, low melting temperature solders (<150°C) for interconnecting components in various applications. However, the current low melting temperature solders face several key challenges, which include more intermetallic compound formation (thus become more brittle), cost issues according to the addition of supplementary elements to decrease the melting point temperature, an increase in the possibility of thermal or popcorn cracking (reliability problems), and so on. Furthermore, the low melting temperature solders are still required to possess rapid electronic/electrical transport ability (high electrical conductivity and current density) and accompany strong mechanical strength sustaining the heavy-uploaded microelectronic devices on the plastic substrates, which are at least those of the conventional melting temperature solders (180–230°C). Thus, the pursuit of more advanced low melting temperature solders for interconnections is timely. This review is devoted to the research on three methods to improve the current properties (i.e., electrical and thermomechanical properties) of low melting temperature solders: (i) doping with a small amount of certain additives, (ii) alloying with a large amount of certain additives, and (iii) reinforcing with metal, carbon, or ceramic materials. In this review, we also summarize the overall recent progress in low melting temperature solders and present a critical overview of the basis of microscopic analysis with regard to grain size and solid solutions, electrical conductivity by supplementation with conductive additives, thermal behavior (melting point and melting range) according to surface oxidation and intermetallic compound formation, and various mechanical properties.

Keywords: heat-sensitive microelectronic components, flexible polymer substrates, low melting temperature solders (<150°C), interconnection applications

1. Introduction

More advanced solder bumps with low melting temperatures are crucial for use in flexible, bendable, and stretchable interconnection technology [1, 2]. In particular, the use of wearable devices requires the development of novel solders that can be reflowed at low temperature to avoid thermal damage to the usually temperature-sensitive components in these flexible devices, such as organic light-emitting diodes (OLEDs), polymer light-emitting diodes (PLEDs), and so on [3–6]. Thus, it is worthwhile to design a low melting temperature solder for more advanced interconnection technology and thus to impart more reliability to the solder bumps between future organic- or polymer-based microchips and flexible substrates. Furthermore, the continuous pursuit of multifunctionality in microelectronics has caused a significant increase in the number of solder bumps, to the level of 10,000 per chip [7]. It also has decreased the bump size to as small as 20 μm [7]. Thus, solder bumps with enhanced electrical and thermomechanical properties are needed to meet these demands. With these uses in mind, the properties of conventional solder materials with high melting temperatures (180–230°C) have been under scrutiny due to their reference characteristics, and whether implementing currently used soldering methods or inventing new ones, solution strategies to overcome problems associated with novel solder materials have been implemented.

In this chapter, we focus on the electrical and thermo-mechanical properties of novel solder materials with a specific range of low melting temperatures (<150°C). Emerging carbon reinforcement materials, such as carbon nanotubes (CNTs), graphenes, and their nanocomposites, are also briefly discussed and linked to the increasing development of composite solder materials (in addition to their low melting temperatures). In particular, strategies for improving the performance of solder materials are proposed, along with the provision of insight into classic metallurgy principles. To engineer the properties of low melting temperature solder materials in intended directions, new approaches using nanostructures, nanocomposites, alloying, and doping are also suggested.

2. Syntheses and/or fabrications of low melting temperature solders

In this section, we show how low melting temperature solders, consisting of various elements with higher melting temperatures, such as Sn (melting point of 231.9°C), In (melting point of 156.6°C), and Bi (melting point of 271.5°C), can be fabricated and/or synthesized using metallurgy principles or nanotechnology theory [8]. For example, the formation of an eutectic alloy with 42 wt.% Sn and 58 wt.% Bi can lead to a melting point decrease to 138°C due to the shift to the eutectic temperature [3, 4]. Due to the melting point drop according to the size decrease, the size reduction effect can also be used to synthesize a low melting point solder [4].

Low melting temperature Sn–In solder nanoparticles were successfully synthesized through a surfactant-assisted one-step chemical reduction method [9]. Different synthesis parameters, including pH, stirring speed, and surfactant concentration, were used to control the size, shape, and uniformity of the Sn–In solder nanoparticles [9]. At low In composition (20 wt.% In), the Sn–In solder nanoparticles were composed of $InSn_4$ alloy and β-Sn phase [9]. When the In content increased to

30 wt.%, the Sn–In solder nanoparticles were composed mainly of $InSn_4$, with a melting temperature of 115.5°C [9]. This low melting temperature indicates a new eutectic point for the Sn–In solder nanoparticle system, which is lower than that of the bulk alloy system (around 50 wt.% In) [9]. At higher In compositions, the Sn–In solder nanoparticles are composed of both $InSn_4$ and In phase [9].

To increase the compatibility and usefulness of the low melting point solder, eutectic Bi–43Sn nanowires with diameters of 20, 70, and 220 nm were fabricated by a hydraulic pressure injection process using anodic aluminum oxide templates [10]. Their microstructure investigation showed that the fabricated nanowires are composed of alternating Bi and Sn segments along the wire axes [10].

Novel Sn–Bi nanocomposites reinforced with reduced graphene oxide nanosheets (RGONs) were successfully fabricated by a simple, scalable, and economical electrochemical deposition method [11]. The Sn–Bi nanocomposites, reinforced with reduced graphene oxide nanosheets, had fine grain size as well as reduced graphene oxide nanosheets dispersed throughout the Sn–Bi matrix [11].

For the microstructural transformation and thermoelectrical improvement of Sn–Bi solder, MWCNT was reinforced using the electrochemical codeposition method [11]. Electron microscopy analysis can confirm that pristine MWCNTs were trapped in the deposited composites [11].

Bi-based solder powders with three chemical compositions (binary Bi–Sn, ternary Bi–Sn–In, and quaternary Bi–Sn–In–Ga alloy systems) were fabricated using a gas atomization technique; subsequently, the powders were further ball-milled to fabricate smaller-sized particulates; in particular, the diameter of those in the Bi–Sn–In–Ga powders became less than 10 μm with an irregular shape due to the nature of intrinsic brittleness, the degree of surface oxidation, and the formation of Ga intermetallic compound (IMC), all of which produced fractures of the Ga-containing powders [3].

Ternary Bi–Sn–In micropowders and nanoparticles were prepared as a composite solder material via gas atomization process and a chemical reduction method, respectively [3, 4]. To be specific, two types of Bi-based micropowders, composed of binary Bi–Sn and ternary Bi–Sn–In, were fabricated using a gas atomizer [4]. Then, the gas-atomized powders were classified using a series of standard sieves to obtain powders of a specific size range [4]. Bi (III) nitrate pentahydrate, Sn (II) 2-ethylhexanoate, In (III) nitrate hydrate at a Bi/Sn/In weight ratio of 43.5/31.5/25.0, and 1,10-phenanthroline were added to methanol, and the solution was stirred for 2 h [4]. Then, sodium borohydride was added, and the reaction continued at 50°C for 1 h [4]. The as-synthesized nanoparticles were centrifuged at 4000 rpm for 15 min, washed with methanol, and then dried in a vacuum oven for 24 h [4].

3. Classification of low melting temperature solders and terminologies for low melting temperature solder design

Conventional, low melting temperature solders are fabricated using either Sn–Bi or Sn–In [12]. In particular, Sn–Bi solders have received considerable attention because of their outstanding

merits, including high wetting behavior, large creep resistance, and low coefficient of thermal expansion [12–14]. However, the relatively low mechanical strength and melting temperature (138°C) of these materials require improvement for their more effective use in flexible interconnection applications [3, 15]. Comparatively, Sn–In solder, which has a low melting temperature (118 °C), has excellent electrical and thermal properties [12, 16]. However, the price of In is very high, and this material includes high amounts of IMCs, which degrade the mechanical properties of the solder [16]. Thus, the incorporation of additives, including alloying, doping, or the use of reinforcement materials, into Sn–Bi or Sn–In alloy systems has been considered a useful strategy for improving the mechanical properties.

3.1. Microstructure with regard to grain size and solid solution

The microstructure reflects the mechanical properties of a solder [15–21]. Based on the microstructural analysis of low melting point solders, specific phases and their distribution in the microstructure can be observed, and these characteristics can be used to describe intended properties [15–21]. In this section, we show how the microstructure of low melting point solders is altered by the incorporation of an additive, especially with regard to grain size and solid solution.

The representative microstructure of eutectic Sn–Bi alloy is shown in **Figure 1**; in this structure, granular Sn-rich grains and similarly granular Bi-rich grains can be seen. The dark and bright gray regions are Sn and Bi, respectively; these regions appear as interlocked lamellar structures. Upon incorporation of an additive into the Sn–Bi solder, the solder microstructure was found to be remarkably transformed due to the formation of finer grains or the presence of new solid solutions or precipitates. Usually, a plausible explanation for this is that Sn- and Bi-rich grains are heterogeneously nucleated in the formation of certain IMCs. For example, Mokhtari et al. demonstrated that the addition of In or Ni can modify the microstructure of Sn–Bi solder; in particular, the addition of 0.5 wt.% In was able to suppress the coarsening of the Bi-rich phase, which means that the Sn–Bi–0.5In solder comprised primary Sn dendrites and eutectic phases [13, 15]. Comparatively, Ni appears to have been included in the Sn phase since Ni-containing Sn–Bi solder exhibited eutectic phases and the Ni_3Sn_4 IMC but did not show any sign of coarsening due to the Bi-rich phase.

Figure 2 exhibits the cross-sectional microstructure of a Sn–40Bi–2Zn–0.1Cu solder alloy composed of Sn-, Bi-, Zn-, and Cu-rich phases. For the cooling (solidification) process of the Sn–40Bi–2Zn–0.1Cu solder alloy from the liquid state, the following procedure took place: L (liquid) → L + primary Sn → primary Sn + eutectic (β-Sn + Bi-rich) + eutectic (β-Sn + Zn-rich) → primary Sn + secondary precipitated Bi + eutectic (β-Sn + secondary precipitated Bi + Bi-rich) + eutectic

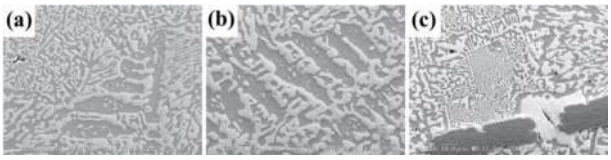

Figure 1. SEM micrographs of (a) eutectic Sn–Bi, (b) Sn–Bi–0.5In, and (c) Sn–Bi–0.5Ni [15].

http://dx.doi.org/10.5772/intechopen.70272

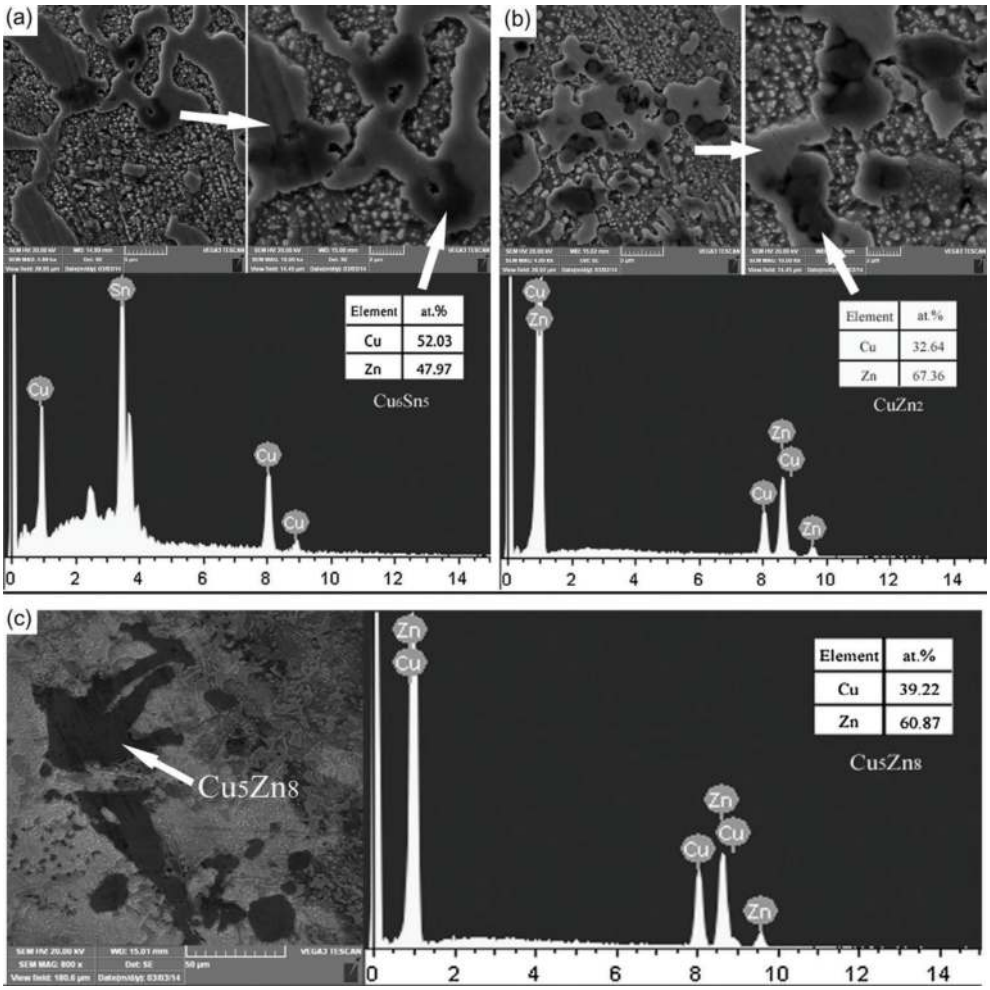

Figure 2. SEM micrograph and EDS analysis results of (a) Cu_6Sn_5 phase in Sn–40Bi–0.1Cu, (b) $CuZn_2$ phase in Sn–40Bi–2Zn–0.1Cu, and (c) Cu_5Zn_8 phase in Sn–40Bi–2Zn–0.1Cu [17].

(β-Sn + Zn-rich). Different from the reference Sn–40Bi–0.1Cu solder alloy, Cu_6Sn_5 precipitates were not found in the Sn–40Bi–2Zn–0.1Cu solder because Cu reacts more strongly with Zn than Sn does; thus, all of the Cu was consumed in the formation of Cu–Zn IMCs [17]. These results were also very similar to the studies of Islam and Li [22, 23]. According to the X-ray diffraction (XRD) and energy dispersive spectroscopy (EDS) analysis, globular $CuZn_2$ and blocky Cu_5Zn_8 precipitates were formed in Sn–40Bi–2Zn–0.1Cu solder; in particular, Zn atoms segregated between the Sn- and Bi-rich matrices and reacted with Cu atoms to form Cu–Zn IMC particles [17].

Figure 3 shows the microstructures of the Sn–58Bi and Sn–Bi–Sb alloys. The Sn–58Bi alloy shows a typical eutectic structure. The dark region is the Sn phase; the white region represents

the Bi phase. For the Sn–Bi–Sb alloys, each part contains two phases, the dark and the light phases shown, respectively, in the images. When the Bi content changes, the proportion of each structure does not greatly change. However, the proportion of quasi-peritectic structure increases, as the Sb content increases [18]. For the Sn–Bi–Sb alloy, the intensity of the Sn-rich phases increased when the Sb content increased [18].

The near eutectic solder (In–50Sn) is presented in **Figure 4a**, showing a cross-sectional microstructure consisting of a combination of lamellar and irregular phases. In particular, the presence of a mixture of Sn-rich and In-rich phases and the In_3Sn IMC was determined by XRD and EDS analyses. Comparatively, **Figure 4b** shows the cross-sectional microstructure of the In–30Sn solder, which consisted of only two specific phases: an In-rich phase and the In_3Sn IMC but the absence of Sn-rich phases and/or other Sn IMCs [16].

As can be seen in **Figure 5**, the interfacial bonding of low melting temperature Sn–In solder on the Cu substrate is presented according to the reflow temperature and duration. The reflow at 180°C for 20 min selected was the optimal condition due to the high bonding strength of 6.5 MPa and the interfacial layer with less microvoids or mechanical cracks [20]. Especially, the reflow temperature of 180°C was high enough for the active diffusion of the low melting

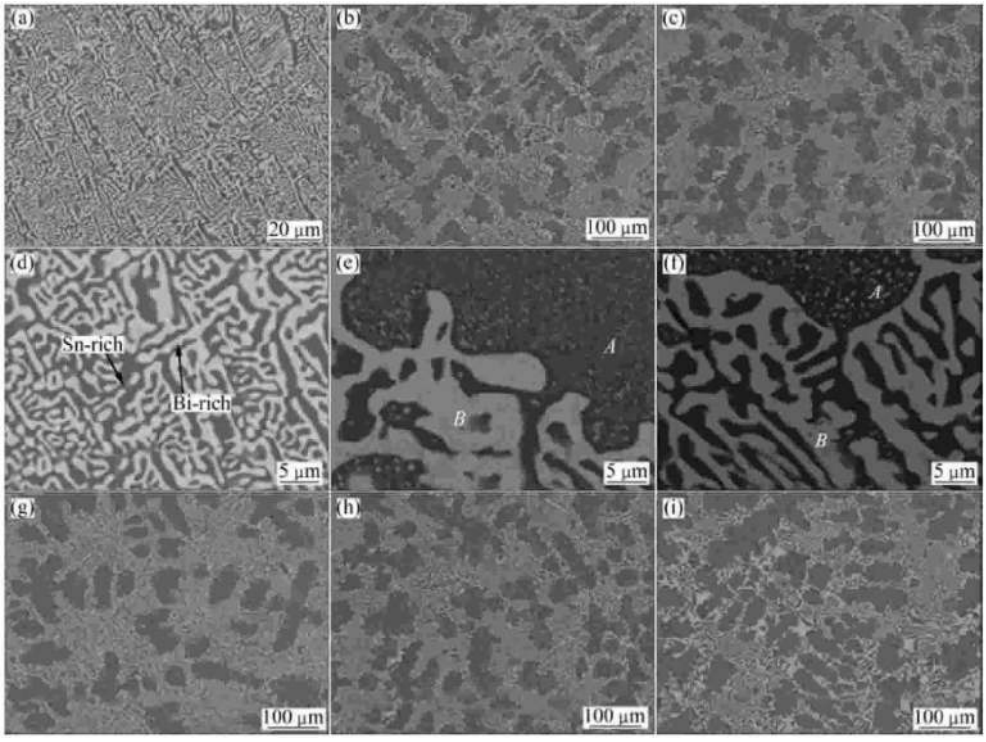

Figure 3. SEM micrographs of Sn–58Bi and Sn–Bi–Sb alloys: (a and d) Sn–58Bi, (b and e) Sn–52Bi–1.8Sb, (c and f) Sn–48Bi–1.8Sb, (g) Sn–48Bi–1.4Sb, (h) Sn–48Bi–1.8Sb, and (i) Sn–48Bi–2.4Sb [18].

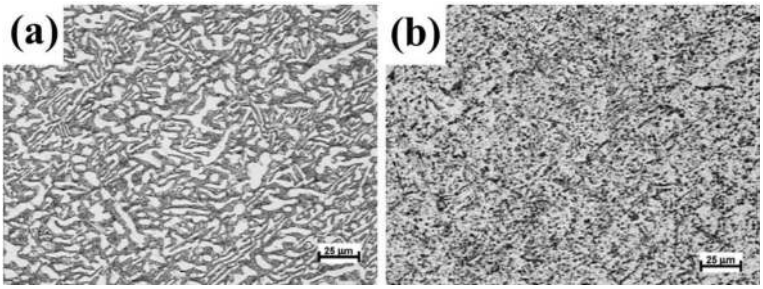

Figure 4. SEM micrographs of (a) In–50Sn and (b) In–30Sn solders [16].

temperature solders, although they were dissolved in the Cu substrates and formed IMCs such as $Cu_6(Sn, In)_5$ and $Cu_{11}(In, Sn)_9$ [20]. Therefore, the joint can sustain high service temperatures because it is formed completely from these IMCs.

Chen et al. determined the interfacial reactions in Sn–51In, Sn–20In, and Sn–20In–2.8Ag on Ag substrates reacted at various temperatures, with results shown in **Figure 6** [21]. Particularly for the Sn–51In/Ag couples, the reaction products are $AgIn_2$ and Ag_2In phases at 150°C and 100°C; only Ag_2In is formed at lower temperatures [21]. Due to the formation of different reaction phases, the reaction layer in the Sn–51In/Ag couples grows more slowly at 100°C than is the case for samples reacted at lower temperatures [21]. The interfacial reaction rates in the Sn–20In/Ag couples are much slower than those in the Sn–51In/Ag couples [21]. In the Sn–20In/Ag couples, the ζ-phase is formed at 250°C, and both ζ-Ag/$AgIn_2$ phases are formed at 125°C; however, no noticeable interfacial reactions are observed to have reacted at 75 and 100°C over a period of 1440 h [21].

The species of IMCs at the interface between the eutectic Sn–In solder and the single crystalline Cu substrate were systematically investigated using scanning electron microscopy (SEM) (**Figure 7**). After reflowing at 160°C for 5 s, two kinds of IMC were formed in three sublayers from the solder to the substrate side; the formed materials were a $Cu(In, Sn)_2$ layer with tetragonal crystal structure, a coarse-grain $Cu_2(In, Sn)$ sublayer, and a fine-grain $Cu_2(In, Sn)$ sublayer with hexagonal crystal structure [24]. The morphology of the $Cu(In, Sn)_2$ grains is chunk type, the largest grain size. In the process of increased liquid soldering, this $Cu(In, Sn)_2$ layer is prone to spalling into the solder, leaving a duplex structure of $Cu_2(In, Sn)$ as the dominating IMC, which should be paid attention during phase identification [24]. The fine-grain $Cu_2(In, Sn)$ shows a granule-type morphology with the smallest grain size; this material distributes homogeneously on the entire Cu substrates [24]. However, coarse-grain $Cu_2(In, Sn)$ is substrate dependent and has an elongated morphology on single crystalline Cu surfaces [24].

The SEM micrographs (**Figure 8**) show Sn–58Bi solders doped with different weight fractions of graphene nanosheets (GNSs). In particular, **Figure 8a** shows the typical lamellar structure of the eutectic Sn–58Bi solder, in which the dark regions represent the Sn-rich phase, while the white regions represent the Bi-rich phase. Compared to the

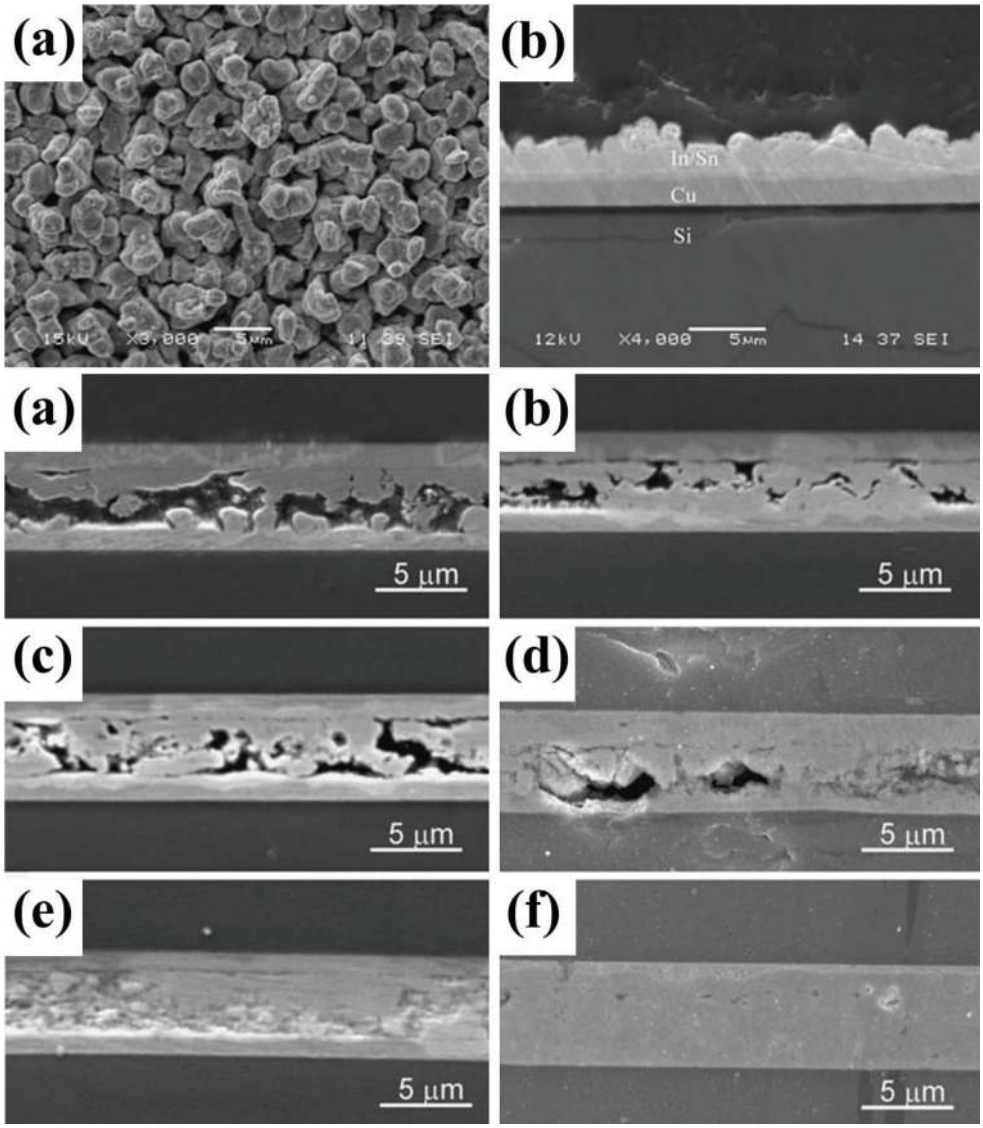

Figure 5. SEM micrographs (top) of as-received coating surface: (a) top view and (b) cross section. Cross-sectional SEM images (bottom) show that at the interfacial layers between the Sn-based solder and the cu substrate, the two components reacted and diffused under the following conditions (reflow temperature (°C) and duration (min)): (a) 140 and 5; (b) 140 and 20; (c) 160 and 5; (d) 160 and 20; (e) 180 and 5; and (f) 180 and 20 [20].

standard Sn–58Bi solder alloy, the microstructure of the composite solder is refined due to the increased content of graphene nanosheets, as shown in **Figure 8b–e**. The average grain size of the pure sample was about 1.6 μm, which is higher than that of the graphene

http://dx.doi.org/10.5772/intechopen.70272

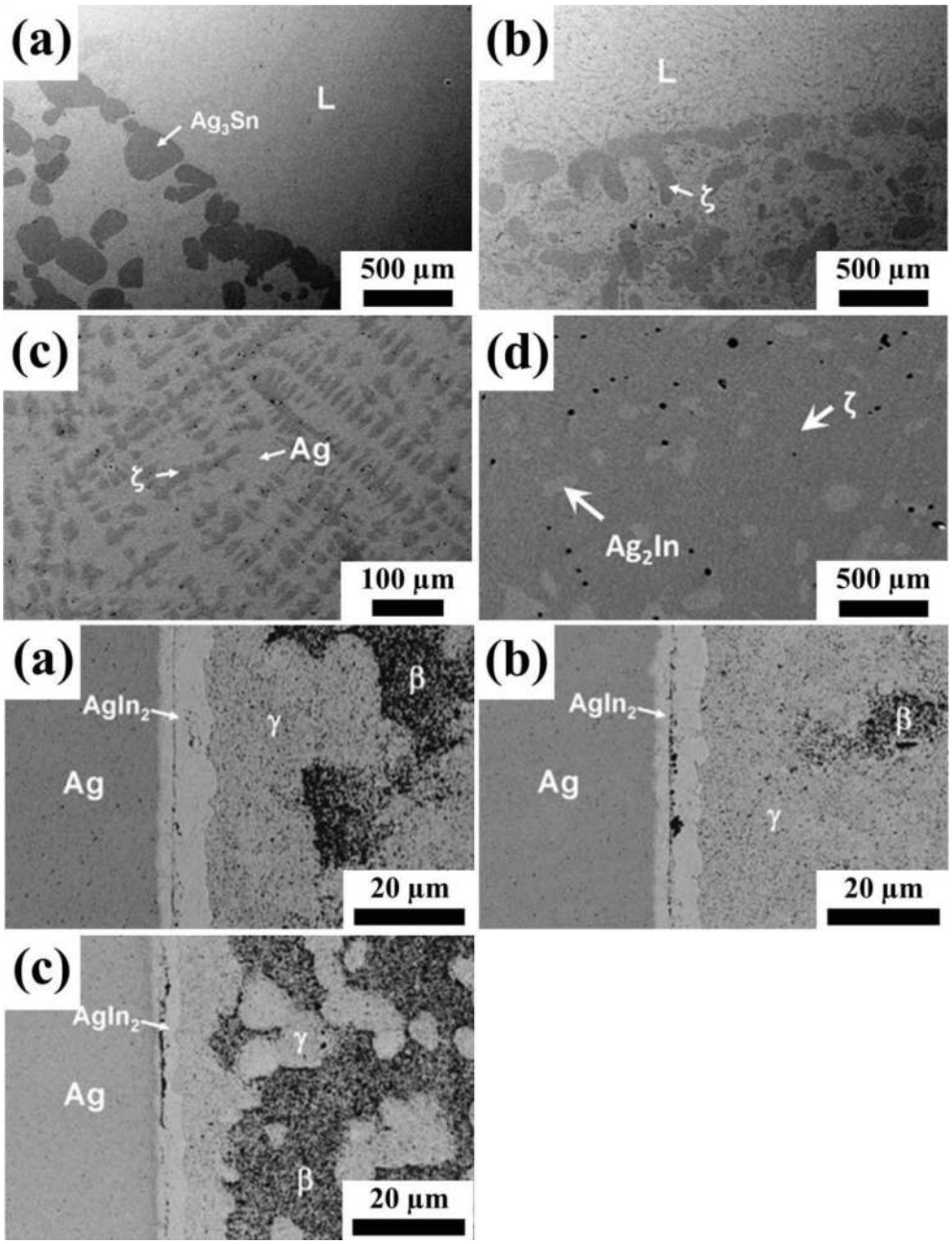

Figure 6. Backscattered electron imaging (BEI) micrographs (top) of (a) Sn–1.98 at.% In–8.03 at.% Ag, (b) Sn–10.02 at.% In–10.01 at.% Ag, (c) Sn–16.99 at.% In–80.01 at.% Ag, and (d) Sn–29.99 at.% In–68.99 at.% Ag annealed at 250°C for 12 weeks. BEI micrographs (bottom) of Sn–51In/Ag couple reacted at (a) 75°C, (b) 50°C, and (c) 25°C for 120 h [21].

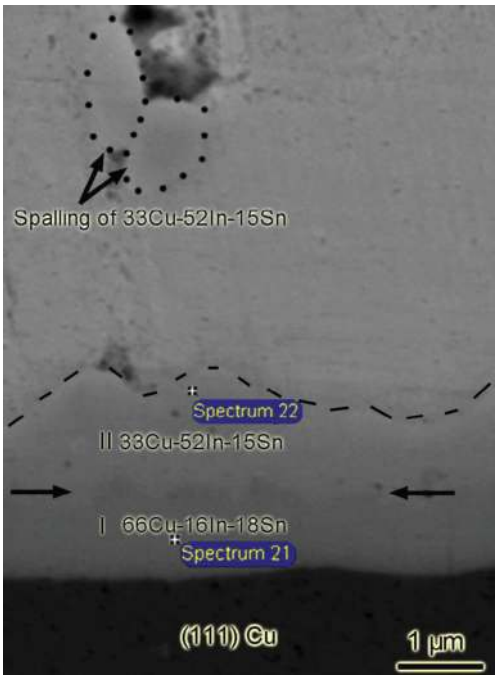

Figure 7. Cross-sectional SEM micrograph at the interface between eutectic Sn–In solder and single crystalline (1 1 1) Cu after reflowing at 160°C for 5 s [24].

nanosheet-doped solder samples [19]. The size reductions of the Sn–58Bi–graphene nanosheet (0.01, 0.03, 0.05, 0.1 wt.%) solders were about 28, 55, 30, and 32%, respectively [19]. These results indicate that the growth of grains was suppressed, and the microstructure of the Sn–58Bi solder alloys was refined by the addition of graphene nanosheets; in addition, the solder alloy with 0.03 wt.% graphene nanosheet addition showed the smallest average grain size [19]. The microstructure of local refinement can be found in **Figure 8b** for the 0.01 wt.% graphene nanosheet addition; meanwhile, uniform refinement of the structure and small Bi grains appear in the Sn–58Bi reinforced with 0.03 wt.% graphene nanosheets, shown in **Figure 8c**. These images indicate that the growth of grains can be suppressed by the presence of graphene nanosheets, which is caused by the high barrier of graphene nanosheets against the diffusion of metal atoms [19]. However, with more graphene nanosheets introduced, the growth of metal grains along the surface of the graphene nanosheets can be promoted [19]. As a result, the distinct feature of the uniformly distributed dendritic structure in Sn–58Bi reinforced with 0.05 wt.% graphene nanosheets can be seen in **Figure 8d**; this structure shows that graphene nanosheets can promote the growth of Bi dendrites. Moreover, local grain aggregation recurs and partial grains growth follows an inverse pattern when the content of graphene nanosheets reaches 0.1 wt.%, as shown in **Figure 8e**. This result is attributed to the increasing addition of graphene nanosheets, which undergo effective bonding with solders [19].

http://dx.doi.org/10.5772/intechopen.70272

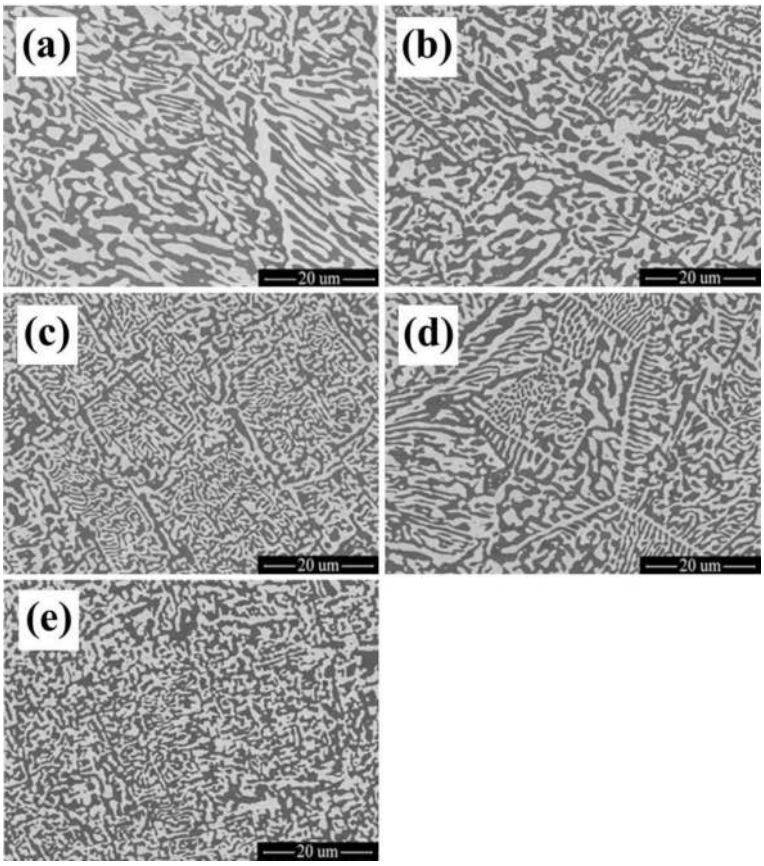

Figure 8. SEM micrographs of (a) Sn–58Bi, (b) Sn–58Bi–0.01GNSs, (c) Sn–58Bi–0.03GNSs, (d) Sn–58Bi–0.05GNSs, and (e) Sn–58Bi–0.1GNSs [19].

3.2. Electrical conductivity modification by supplementation with conductive additives cd, Sb, cu, Ag, Zn, in, Ni, and carbon nanomaterials

The solder bump size on a packaging substrate decreases as a result of the electronic components being miniaturized [25–28]. Simultaneously, the pitch distance drops to the submicron level [27, 28]. The pin count increases to meet the demands of rapid signal transmission and high current load [28]. Thus, the electrical property of a solder becomes one of the most important factors [29–31]. In the literature, however, there is not much research on the electrical properties of low melting point solders. Thus, determining the electrical property for a low melting point solder can be of great use to researchers and engineers, especially those who design solder alloys. Meanwhile, the eutectic Sn–Bi solder has a relatively high electrical resistivity of 30–35 μΩ·cm due to the electrical resistivity of Bi (115 μΩ·cm), while the eutectic Sn–In solder has a very low electrical resistivity of 10–15 μΩ·cm due to the electrical resistivity of In (8 μΩ·cm) [30].

Altıntas et al. determined that the electrical conductivity varies with temperature for low melting point solders: Sn–41.39 at.% Cd–6.69 at.% Sb, Sn–49 at.% In–1 at.% Cu, Sn–50 at.% Ag–10 at.% Bi, and Sn–32 at.% Bi–3 at.% Zn alloys; these values were determined by the four-point probe method, as shown in **Figure 9** [31]. The electrical conductivities of all solder alloys in the present work were found to decrease linearly with increasing temperature. The electrical conductivity values as a function of temperature were found to be in ranges of 4.35–2.76, 5.00–3.43, 5.30–4.58, and 1.52–1.39 ($\times 10^6$)/Ω·m for Sn–Cd–Sb, Sn–In–Cu, Sn–Ag–Bi, and Sn–Bi–Zn solder alloys, respectively [31]. By extrapolating the electrical conductivity lines to their melting temperature, values of electrical conductivity for Sn–Cd–Sb, Sn–In–Cu, Sn–Ag–Bi, and Sn–Bi–Zn at their melting temperatures were determined to be 2.61, 3.26, 4.57, and 1.35 ($\times 10^6$)/Ω·m, respectively, as shown in **Table 1**.

Figure 10 depicts the resistivity of all Sn–Bi solder alloys according to the increase of the Ni amount. No significant change in the electrical resistivity was detected following the addition of Ni. Although the existence of IMCs in the solders could induce a higher electrical resistivity, in this research the effect on the solders' electrical resistivity in the presence of Ni_3Sn_4 is not apparent [29].

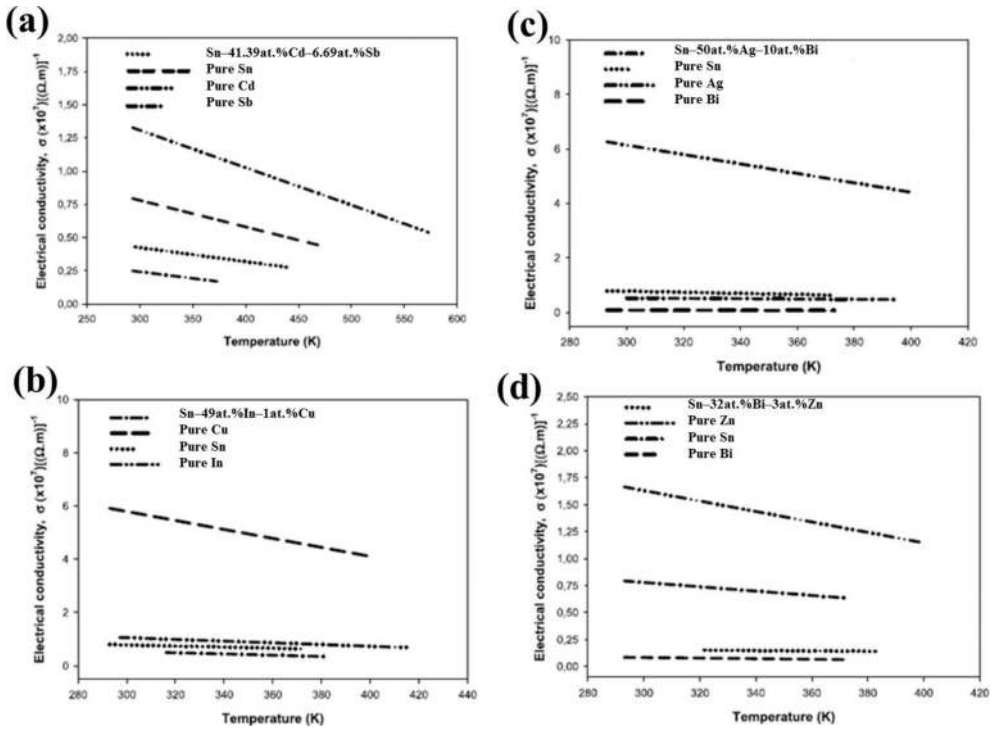

Figure 9. Electrical conductivity measurements according to temperature for (a) Sn–41.39Cd–6.69Sb, (b) Sn–49In–1Cu, (c) Sn–50Ag–10Bi, and (d) Sn–32Bi–3Zn (at.%) solder alloys [31].

	Melting temperature (K)	Temperature coefficient of σ (K^{-1}) × 10^{-3}	σ at the melting temp (1/Ω·m) × 10^{6}
Sn–41.39 at.% Cd–6.69 at.% Sb	453	2.47	2.61
Sn–49 at.% In–1 at.% Cu	389	4.97	3.26
Sn–50 at.% Ag–10 at.% Bi	411.4	1.14	4.57
Sn–32 at.% Bi–3 at.% Zn	404.7	1.00	1.35
Sn–4 wt.% Ag–2 wt.% In	490.7	–	–
Sn–20 wt.% Ag–2 wt.% In	490.7	–	–
Sn–40 wt.% Ag–2 wt.% In	490.7	–	–
Sn–20 wt.% In–25 wt.% Ag	490.7	–	–
Sn–20 wt.% In–10 wt.% Ag	490.7	–	–
Sn–20 wt.% In–15 wt.% Ag	486.0	–	–
Sn–6 wt.% Sb–5 wt.% Ag	507.8	–	–
Sn–42.8 wt.% Bi–0.04 wt.% Cu	411.8	–	–
Sn–3.5 wt.% Ag–0.9 wt.% Cu	490.2	–	–

Table 1. Some electrical properties of solid phase for Sn–41.39 at.% Cd–6.69 at.% Sb, Sn–49 at.% In–1 at.% Cu, Sn–50 at.% Ag–10 at.% Bi, Sn–32 at.% Bi–3 at.% Zn [31].

The incorporation of carbon nanomaterials with graphene structures can also impart much more rapid electron transfer than that can be obtained using conventional Sn–Bi solder [32]. Subsequently, reinforcement with carbon nanomaterials having high thermal conductivity can be used to tailor a network structure to effectively transfer the outer thermal energy to the solder matrix [32]. **Figure 11** shows the calculated current efficiency versus different MWCNT additions in the solder alloy. This implies that the current efficiency is dependent on the concentration of

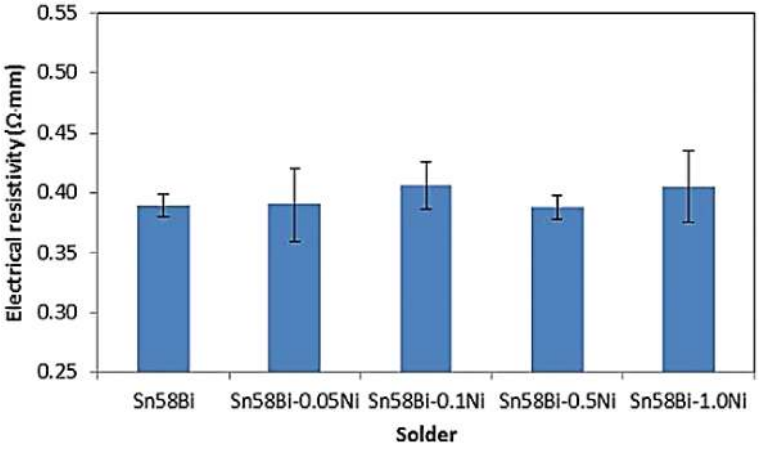

Figure 10. Electrical resistivity of Sn–58Bi–xNi [29].

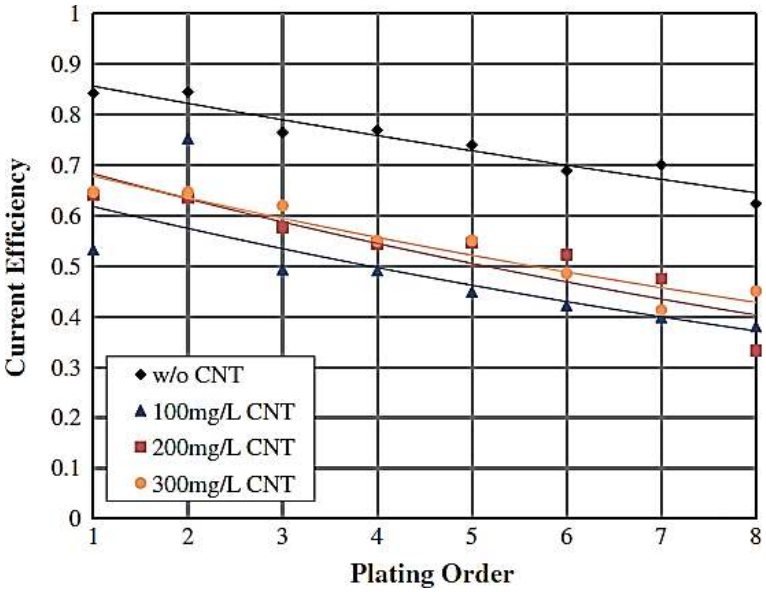

Figure 11. Current efficiency change of the Sn–Bi solder under CNT load [32].

the solder constituent electrolytes [32]. This is mainly due to the increased hydrogen evolution caused by lower ion concentration in the vicinity of the nucleation/deposition sites [32]. On the other hand, the addition of MWCNTs into the solder alloy reduces the current efficiency because pristine MWCNTs are trapped in the deposited composites [32]. Due to the bridging effects of trapped MWCNTs, the Sn–Bi–CNT composite is denser than the pure Sn–Bi alloy [32].

3.3. Thermal behavior (melting point and melting range) according to surface oxidation and intermetallic compound formation

Near-future generations of electronics are expected to be flexible, bendable, and wearable [1]. The use of flexible devices requires the development of a novel solder that can be reflowed at a low temperature to avoid thermal damage to these flexible devices, which usually have temperature-sensitive components [3, 4]. In addition, the melting point of a solder alloy should be the first priority for consideration when it comes to the manufacturing process [3, 4]. Meanwhile, the eutectic point (usually, the low melting point) in a binary phase diagram is where a liquid phase and two solid phases can coexist at equilibrium. Thus, a large number of low melting point solders with eutectic compositions are mostly used for flip chip solder joint applications between microchips and substrates.

Figure 12 shows the solidus and liquidus temperatures, and the differences between both temperatures, referred to as the melting range of Sn–58Bi–xNi (x = 0.05, 0.1, 0.5 and 1.0 wt.%) solder alloys. The addition of Ni apparently lowered the solidus and liquidus temperatures [29]. This phenomenon was attributable to the fact that the addition of small amounts of Ni altered the composition of the alloy to resemble the eutectic composition of the ternary Sn–Bi–Ni alloy system [29].

http://dx.doi.org/10.5772/intechopen.70272

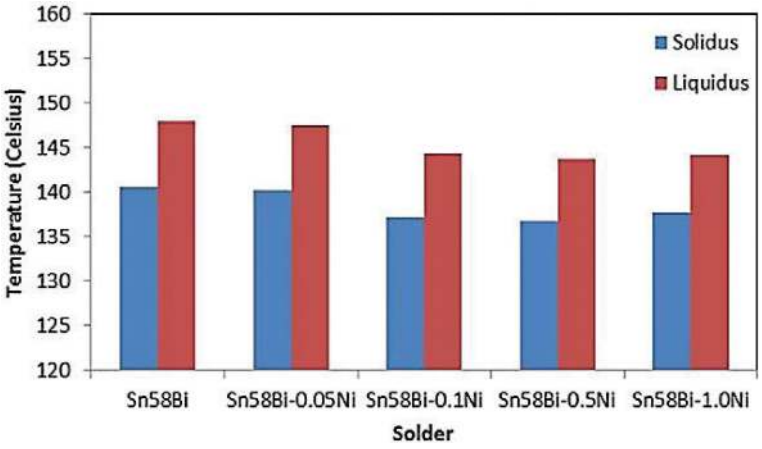

Figure 12. Solidus and liquidus temperatures of Sn–58Bi–xNi [29].

Using the differential scanning calorimetry (DSC), when the content of In was increased to 23.8 wt.%. Kim et al. determined that the prominent endothermic peak of the Bi–Sn–In powders shifted to 82.0°C from that of the Bi–Sn powders, which have a peak at 139.6°C [3, 4]. The continuous addition of 4.8 wt.% Ga shifted the peak even more to 60.3°C. Meanwhile, there was a slight broadening in the solidus line of the melting peak of the Bi–Sn–In solder powders mainly due to the formation of an In-rich phase [3]. Furthermore, the formation of new Ga0.9In0.1, BiIn, and In0.2Sn0.8 IMCs according to the addition of 4.8 wt.% Ga to the Bi–Sn–In solder alloy system also influenced the melting range broadening [3]. Kim et al. also show that ternary Bi–Sn–In nanoparticles, with a 71.1°C melting temperature, entered among the intervals of the higher melting temperature (79.4°C) micropowders and then reflowed at 110°C on a flexible polyethylene terephthalate (PET) substrate [4].

The fundamental thermal properties of Sn–58Bi–xZn (x = 0 and 0.7 wt.%) solder alloys were also analyzed by DSC, with results as shown in **Figure 13**. The results indicate that the solidus temperature of solder alloys slightly decreased with the addition of Zn content [33]. The reduction in solidus temperature of solders can probably be attributed to the increase in the surface instability due to the higher surface energy induced by the addition of Zn [33].

As can be seen in **Figure 14a**, the eutectic solder (In–Sn) had a low melting point of 118.5°C and a narrow melting range. The DSC curves of the hypo-eutectic Sn–70In and eutectic Sn–Bi solders were also presented in **Figure 14b** and **c**, respectively. In addition, the Bi53–Sn26–Cd21 solder presented in **Figure 14d** had the lowest melting temperature and a narrow melting range; thus, this solder had more active phase transformation than the others. The solidus temperatures, liquidus temperatures, and mushy temperature zones of Sn–58Bi, Sn–40Bi–0.1Cu, and Sn–40Bi–2Zn–0.1Cu solder alloys are collected in **Table 2**. The melting peak of the eutectic Sn–Bi solder decreased from 139.0 to 132.2°C according to the addition of a small amount of Cu; however, the addition of 2 wt.% Zn into the Cu-containing solder imparted a slight increase in the melting point (136.3°C) of

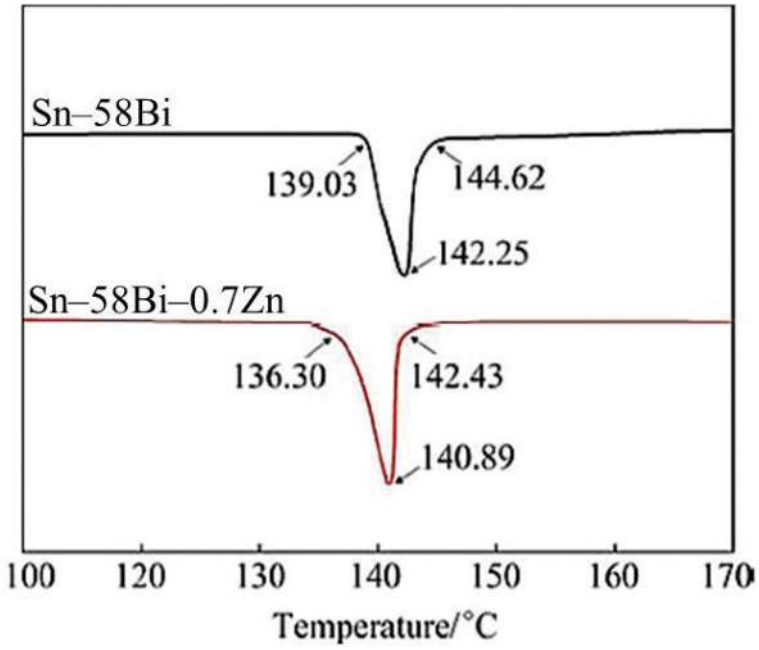

Figure 13. DSC curves of Sn–58Bi–xZn (x = 0 and 0.7) solders [33].

the Sn–40Bi–2Zn–0.1Cu solder [17]. Thus, the addition of Cu decreased the melting point of the Sn–Bi-based solder, while the addition of Zn provided the reverse effect (melting temperature increase) [17]. Moreover, Cu addition decreased the melting range of the Sn–Bi-based solder from 27.2 to 22.0°C, while the addition of Zn to Sn–40Bi–2Zn–0.1Cu increased the melting range slightly to 23.1°C [17]. The thermal conductivity of the Sn–40Bi–2Zn–0.1Cu solder of 24.51 W/(m·K) was the highest, while the Sn–40Bi–0.1Cu solder took second place with a value of 20.48 W/(m·K). Zn and Cu additions obviously improved the thermal conductivity of the Sn–Bi-based solder alloy [17]. Aksoz et al. reported that the thermal conductivity of pure Zn is 116 W/(m·K), which is higher than those of pure Bi (8 W/(m·K)) and pure Sn (67 W/(m·K)) [34]. This is the reason that the Sn–40Bi–2Zn–0.1Cu solder has the highest thermal conductivity [34]. The temperatures of the endothermic peaks of the nine Sn–Bi–Sb alloys are shown in **Table 3**. All the main peaks appear at around 147°C. The melting range of all the Sn–Bi–Sb alloys is larger than that of the eutectic alloy [18]. Side peaks are observed in many DSC profiles of the Sn–Bi–Sb alloys [18]. As the Bi content is reduced, the melting range obviously becomes large. Meanwhile, the melting range and the liquidus temperature reached maximum values for the composition of Sn–48Bi–1.8Sb and then started to drop when Sb content changed [18]. The melting range may be attributed to the fact that the proportion of the eutectic structure will change when Bi or Sb content changes [18]. For the liquidus temperature, it was found that the primary phase changes to the β-Sn phase, when the Sb content is more than 1.8% [18]. The presence of second phase implies that the remaining primary phase continues to melt after quasi-peritectic reaction [18].

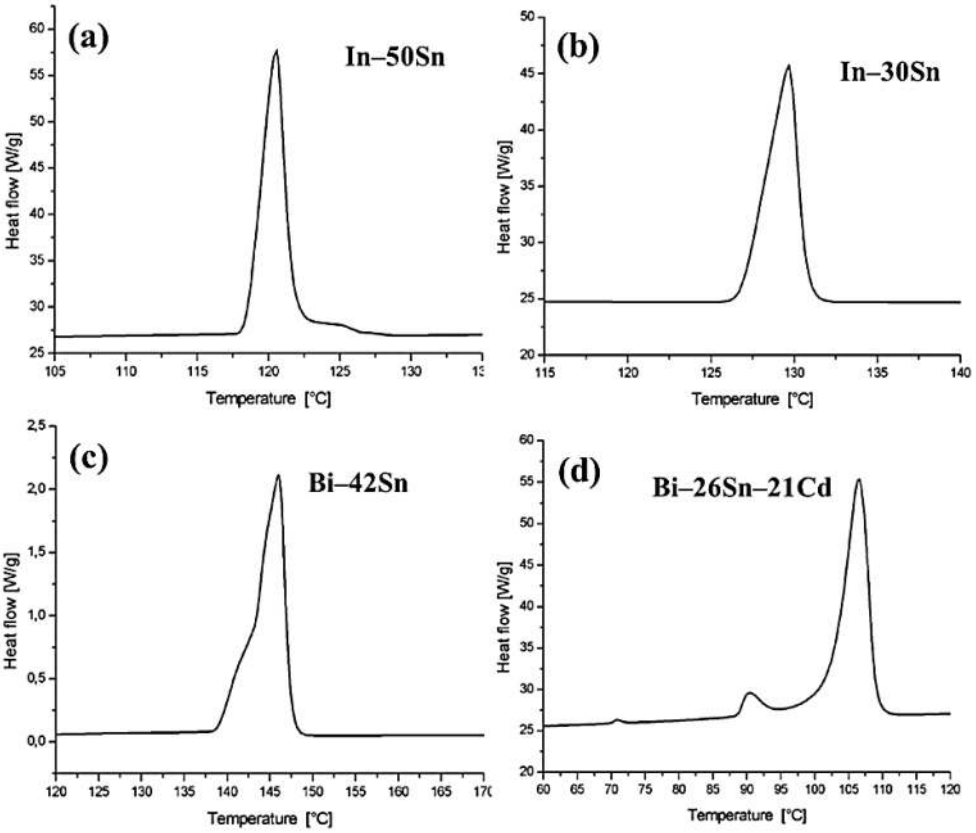

Figure 14. DSC curves of (a) In–50Sn, (b) In–30Sn, (c) Bi–42Sn, and (d) Bi–26Sn–21Cd solders [16].

Composition (wt.%)	Solid temperature (°C)	Liquid temperature (°C)	Pasty range (°C)	Mean TC (W/(mK))
Sn-58Bi	130.2	157.4	27.2	17.43 ± 0.6
Sn-40Bi-0.1Cu	125.1	147.1	22	20.48 ± 0.3
Sn-40Bi-2Zn-0.1Cu	127.7	150.8	23.1	24.51 ± 0.8

Table 2. Solidus temperatures, liquids temperatures, melting ranges, and mean thermal conductivity of the solder alloys [17].

Figure 15 shows the variation of the melting point of composite solder alloys with different dopant contents (both CNTs and Ni–CNTs) compared to the melting point of the Sn–57.6Bi–0.4Ag solder (about 140°C). It can be found that all the melting points were within the range of 139.3–139.6°C [35]. It has been reported that both CNTs and Ni–CNTs have an effect of reducing the melting point of solder alloys [35]. In particular, with the combined effect of CNTs and Ni–CNTs doped Sn–57.6Bi–0.4Ag solder alloys showed relatively lower melting points than those of CNTs doped solder alloys [35]. However, such small additions of CNTs and Ni–CNTs cannot have a significant influence on the melting point of Sn–57.6Bi–0.4Ag solder alloy [35].

Composition (wt.%)	Main peak temperature (°C)	Sec peak temperature (°C)	Solid temperature (°C)	Liquid temperature (°C)	Melting range (°C)
Sn–58Bi	143.1		139.4	148.0	8.6
Sn–52Bi–1.8Sb	147.7		140.6	152.0	11.4
Sn–48Bi–1.8Sb	146.5	163.0	140.9	172.7	31.8
Sn–44Bi–1.8Sb	146.9	169.0	141.9	180.5	38.6
Sn–48Bi–1.0Sb	144.7	162.0	140.6	168.7	28.1
Sn–48Bi–1.4Sb	146.8	163.3	141.2	170.4	29.2
Sn–48Bi–1.8Sb	146.5	163.0	140.9	172.7	31.8
Sn–48Bi–2.0Sb	147.6	164.4	142.3	169.7	27.4
Sn–48Bi–2.4Sb	148.5	163.3	142.8	169.3	26.5
Sn–48Bi–2.8Sb	148.0	162.6	143.6	168.4	24.8

Table 3. Thermal behaviors of standard Sn–58Bi alloy, Sn–52Bi–1.8Sb alloys, and Sn–48Bi–xSn alloys [18].

Figure 16 shows the DSC endothermic peaks of Sn–Bi nanocomposites reinforced with 0.02 or 0.05 g of reduced graphene nanosheets. While a large endothermic peak corresponding to the melting reaction in the range of 139.0°C of Sn–Bi solder has been observed, it was found that the melting point of Sn–Bi nanocomposites reinforced with reduced graphene nanosheets was about 139.0°C, which indicates that there was no significant effect on the thermal behavior of the nanocomposite solder, despite of the addition of reduced graphene nanosheets [11].

3.4. Mechanical properties

The durability and reliability of electronic products, as related to the mechanical properties of the solder joints, have become very important [13, 36–41]. This is especially true for portable, wearable devices, which frequently experience mechanical shock loadings caused by external forces [4]. Particularly for drop tests, during which the strain rate is very high, high mechanical shock resistance of solders is needed for these materials to fulfill their roles of structural materials. In addition, low melting point solders experience significantly high stresses during the reflow process owing to thermal gradient difference [3, 4]. Thus, there has been continuous interest in better understanding of the mechanical properties and in inventing high durability and reliability low melting point solders. One frequently utilized way to influence the mechanical properties of low melting point solder joints in a given system is to either alloy the materials or add small or large amounts of additional elements. In particular, any metal oxides or impurities may have marked effects on the mechanical properties of low melting point solders. Additional elements can fundamentally influence the mechanical properties of low melting point solders. First, additional elements can have an influence on the mechanical properties of the interfacial reactions between the solder and the substrate. Second, additives can positively change the mechanical properties of low melting point solders. Third, they can impart negative side effects, which result in a sacrifice of other mechanical properties of low

http://dx.doi.org/10.5772/intechopen.70272

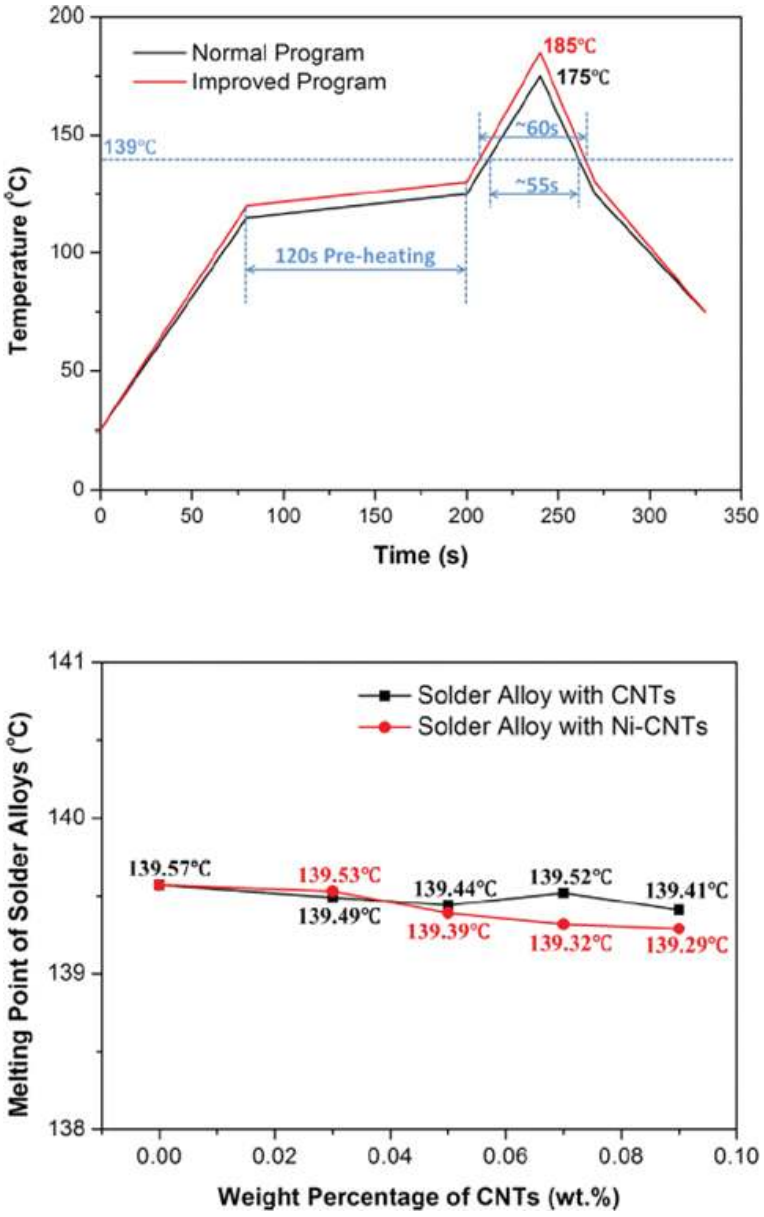

Figure 15. Plot of the variation of melting point of solder alloys with different amounts of CNTs or NI–CNTs [35].

melting point solders. In this section, therefore, we report on a number of investigations about the effects of different alloying elements, as well as the effects of metal oxides or impurities, in low melting point solders.

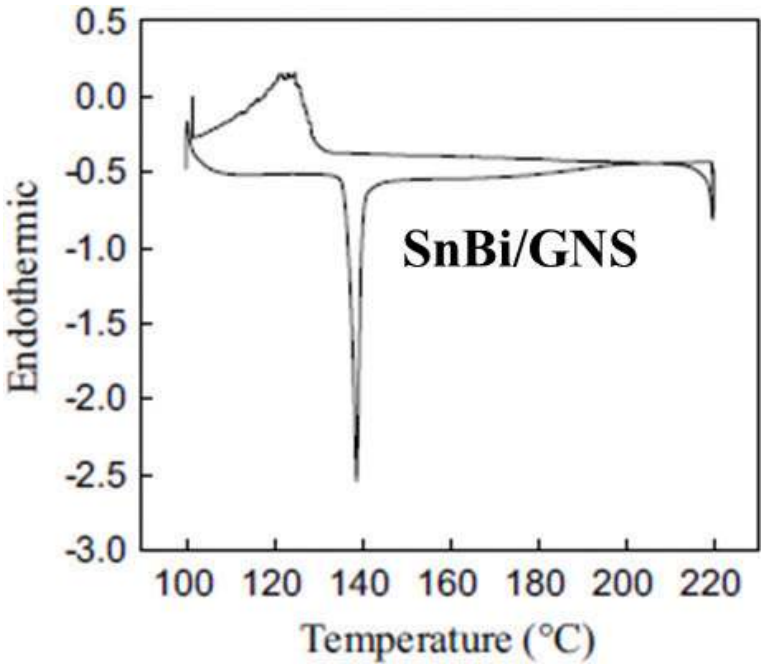

Figure 16. DSC of Sn–bi/RGOS nanocomposites with Sn content of 36.0 wt.% [11].

After the addition of 0.05 wt.% Cu_6Sn_5 nanoparticles in Sn–Bi solder, the tensile properties of the solder underwent brittleness caused by a change in ductility [36]. However, nanoindentation testing revealed that the creep resistance of the Sn–Bi–Cu_6Sn_5 solder is enhanced through the creep mechanism transformation [36]. In corrosion experiments, samples with Cu_6Sn_5 nanoparticles exhibit a lower corrosion rate [36].

Adding different sized Ag nanoparticles to a eutectic Sn–Bi alloy system refined the grain (microstructure), suppressed the growth and expansion of the interfacial IMCs, and increased the shear strength of the solder joint [38]. To be specific, the reinforcement with 76 nm Ag nanoparticles refined the microstructure by 49.1% and enhanced the microhardness by 12.2% compared to the standard Sn–Bi solder because the extent of the formation of the Cu–Sn IMC decreased from 0.394 to 0.339, suppressing the IMC thickness by 39.7% and improving the shear strength by 18.9% after reflowing at 220°C for 180 min. However, after the addition of both larger (133 nm) and smaller (31 nm) Ag nanoparticles, such thermomechanical properties improvements were lower than those of the solder having 76 nm Ag nanoparticles [38]. These improvements might have been due to refinement and dispersion strengthening and adsorption [38]. In fact, although the solder with smaller Ag nanoparticles should have had higher property improvements than those with larger ones, the agglomeration of the smaller sized Ag nanoparticles deteriorated the overall solder's properties and reduced the practical improvements [38]. Overall, an optimal particle size was proposed to balance the theoretical improvement and the agglomeration weakening; this size generated the best real improvement [38].

http://dx.doi.org/10.5772/intechopen.70272

The reinforcement effects of the Al_2O_3 nanoparticles in Sn–58Bi solder were investigated from the aspects of electromigration, shear strength, and microhardness [39]. The experimental results show that the Al_2O_3 nanoparticles significantly improved the mechanical performances of the solder joints. The addition of Al_2O_3 nanoparticles reduced the thickness of the Bi IMCs along the interfacial layers [39]. More specifically, the growth rate of the IMC thickness according to the addition of Al_2O_3 nanoparticles decreased by 8% compared with that of pristine solder [39]. Furthermore, the microhardness of Al_2O_3-containing solder exhibited better performance than that of pristine solder according to aging time [39]. On the other hand, the addition of Al_2O_3 significantly improved the shear strength of the solder joint after aging for 48 and 288 h [39]. More specifically, after the solder was aged for these time periods at 85°C, the amplitudes of the shear strength increased by 3.5% and 2.4%, respectively, because unlike the smooth surface of the pristine solder, the surface of the Al_2O_3-containing solder showed a ductile failure (fractured) state [39].

To improve the mechanical behaviors of a Sn–58Bi/Cu joint, a minor amount of elemental Zn was alloyed into the Cu substrate [40]. The interfacial IMC growth and bending properties of Sn–58Bi/Cu and Sn–58Bi/Cu–2.29Zn were studied according to the effect of isothermal liquid and solid aging [40]. Although there was no significant change in the composition, thickness, or morphology of the interfacial IMC under liquid aging, the depressing of IMC growth at the interface between the Sn–58Bi solder and the substrate and the avoidance of the formation of Cu_3Sn IMC, Kirkendall voids, and Bi segregation at the IMC/Cu interface were realized for the Cu–Zn substrate under isothermal solid aging [40]. Joint strength and fracture behavior were also improved when using the Cu–Zn substrate [40]. There was no obvious decrease in the joint strength, and fracturing during bending was found mainly to occur in the solder matrix with ductile fracture mode or along the solder/IMC interface with partly brittle fracture mode for the Cu–Zn joint; these behaviors can be compared with the dramatically decreased joint strength and brittle fracture mode that occurred along the interface between IMC and Cu in Sn–Bi/Cu joints after aging [40].

Sn–57.6Bi–0.4Ag solder was reinforced with tungsten (W) nanoparticles at a concentration of 0.5 wt.% [41]. Due to the dispersion of W nanoparticles and the consequently refined microstructure, the mechanical properties of the solder alloy were enhanced, as indicated by the 6.2% improvement in the microhardness [41]. During electromigration, the segregation of the Sn-rich and Bi-rich phases and the accumulation of an (Au, Ni), $(Sn, Bi)_4$ layer at the cathode interface were also alleviated by the addition of W nanoparticles, which improved the electromigration resistance [41].

The tensile properties of eutectic Sn–Bi, Sn–Bi–0.5In, and Sn–Bi–0.5Ni solder alloys, and their shear strength as Cu/solder/Cu joints were investigated [15]. The addition of 0.5 wt.% Ni decreased the elongation property of the Sn–Bi alloy because of the formation of Ni_3Sn_4 IMCs [15]. The In-bearing solder alloys exhibited the greatest elongation among all the tensile-tested solder alloys [15]. The eutectic Sn–Bi and Ni-bearing solder joints exhibited degraded shear strength owing to the formation of coarsened Bi-rich phases [15]. The thermally aged Sn–Bi solder joints on Cu substrates exhibited a harshly fractured surface structure in the IMC layers at the interfacial boundaries, whereas the thermally aged In- and Ni-containing Sn–Bi solder

joints showed a smoothly fractured surface structure because of the growth suppression of Cu–Sn IMCs [15]. In particular, the as-reflowed In-containing solder joints had a dimple-like, fractured surface structure, indicating a ductile microstructure because the thermally aged In-containing solder joints retained their ductile property well, while both the coarsened, fractured surface structure and excessive IMC growth of the thermally aged Sn–Bi solder joints at the interfacial boundaries is able to explain their mechanical degradation [15].

Four different concentrations of Ni (i.e. 0.05, 0.1, 0.5, and 1.0 wt.%) were individually added to Sn–58Bi samples, and respective microstructure, tensile strength, elongation, and wettability of Sn–58Bi–xNi were subsequently measured [29]. The results indicate that Ni refined the microstructure of the solder matrix and induced the formation of the Ni_3Sn_4 phase; furthermore, the formation and then continuously increasing concentration of Ni_3Sn_4 were proportional to the increase of Ni added to the solder [29]. Thus, the optimal concentration of Ni added to enhance the solder's tensile strength should be less than 0.1 wt.% [29]. Nevertheless, the elongation of the alloy was in fact inversely proportional to the increase of the added Ni content, although the appropriate incorporation of Ni contributed positively to the wettability of the solder alloy [29].

When the In content increased to 4% in the Sn–Bi alloy, tensile test results showed that the tensile strength increased slightly with the increase of added In, while the elongation first increased remarkably and then decreased after the addition of 2.5 wt.% In [13]. The diffused In was confirmed to participate in interfacial reactions, thereby forming Cu–Sn–In IMCs and affecting the wettability of the Sn–Bi solder on the Cu substrate [13]. Tensile strength changed slightly with increasing In addition, while the elongation increased remarkably with the addition of 2.5 wt.% In [13].

The interfacial reaction kinetics, tensile strength, and creep resistance of the Sn–58Bi–xZn (x = 0.0 or 0.7 wt.%) solder samples during liquid-state aging were investigated [33]. With the addition of 0.7 wt.% Zn, ultimate tensile strength (UTS) values of the eutectic Sn–Bi solder increased by 6.05 and 5.50% after soldering and aging, respectively; those values for the Cu/Sn–Bi/Cu solder joints also increased by 21.51 and 29.27%, respectively [33]. The increase in strengthening of the Cu/Sn–Bi–xZn/Cu solder joints can be attributed to the phase transformation at each Cu/IMC/solder interface due to the formation of finer Bi grains according to the addition of Zn [33].

The effect of Sb content on the mechanical properties of Sn–Bi solders was studied [18]. The mechanical properties of the solders/Cu joints were also evaluated [18]. The results show that the ternary alloy solders contain eutectic structures resulting from a quasi-peritetic reaction [18]. With the increase of the Sb content, the size of the eutectic structure increases [18]. A small amount of Sb has a large impact on the wettability of the Sn–Bi solders [18]. Reaction layers form during the spreading process [18]. Sb is detected in the reaction layer, while Bi is not detected [18]. The total thickness of the reaction layer between the solder and Cu increases with increased Sb [18]. The shear strength of the Sn–Bi–Sb solders also increases as the Sb content increases [18].

http://dx.doi.org/10.5772/intechopen.70272

The mechanical properties of the melt-spun Bi–42Sn, Bi–40Sn–2In, Bi–40Sn–2Ag, and Bi–38Sn–2In–2Ag alloys were studied using dynamic resonance and Vickers indentation techniques at room temperature and compared to the mechanical properties of the traditional Sn–Pb eutectic alloy [42]. The results show that the crystallographic structure of the Bi–42Sn alloy presents as a combination of body centered tetragonal Sn and rhombohedral Bi [42]. The two ternary alloys exhibit additional constituent phases of $SnIn_{19}$ for Bi–40Sn–2In and Ag_3Sn for Bi–40Sn–2Ag alloys [42]. Attention has been paid to the role of IMCs in the mechanical and creep behavior [42]. The In- and Ag-containing solder alloys exhibited a good combination of higher creep resistance as compared with the Pb–Sn eutectic solder alloy [42]. This was attributed to the strengthening effect of Bi in the Sn matrix and the formation of $InSn_{19}$ and Ag_3Sn IMCs, which act as grain refiners in the matrix material [42].

Sn–57.6Bi–0.4Ag solder joints with different contents of CNTs and Ni–CNTs were investigated [35]. In particular, it was possible to improve the mechanical properties of the Sn57.6Bi0.4Ag solder joints by the addition of either CNTs or Ni–CNTs, and those with the addition of 0.05 wt.% CNTs or 0.07 wt.% Ni–CNTs showed the best mechanical performance [35]. With the addition of either CNTs or Ni–CNTs, the solder joints had rougher, fractured surface structures, resulting in better bonding properties. Although reinforcement with either CNTs or Ni–CNTs improved the mechanical performance of solder joints, Ni–CNTs worked much better [35]. Ni coating was proven to significantly inhibit the aggregation of CNTs, which can induce cracks and wetting problems and even deteriorate the strength of solder joints [35].

Sn–Bi composite solders containing Ni–CNTs were successfully synthesized [43]. The mechanical properties of Sn–Bi with different weight percentages of Ni–CNT were investigated [43]. The UTS and elongation of the Sn–Bi–0.05(Ni–CNT) solder with the optimized amount (0.05 wt.%) of Ni–CNTs increased remarkably because the CNTs and Ni_3Sn_4 enhanced the wettability and bondability of the composite solder [43]. However, because of the presence of CNT clusters and the intrinsic brittleness of IMCs, the UTS and elongation degraded with increased addition of Ni–CNTs [43]. That is to say, the UTS of the solder joint reached its maximum value with 0.05 wt.% Ni–CNTs addition and then degraded after increased addition of Ni–CNT [43]. Moreover, the tensile strength of the composite solder was much higher than that of the pristine solder, and subsequently, the creep resistance and hardness of the Sn–Bi–0.05(Ni–CNT) solder increased significantly compared to those of the Sn–Bi solder [43]. However, the hardness and the creep performance also decreased with 0.1 and 0.2 wt.% CNT content due to the same reasons mentioned above [43]. The CNT clusters and pore formation in the presence of the IMC with its intrinsic brittleness contributed to the decreases of hardness and creep performance [43].

The mechanical strength and ductility of the eutectic Sn–Bi solder alloy were dependent on the incorporation of MWCNTs [44]. Mechanical test results show that the bending strength of the Sn–Bi–0.03CNT composite increased by 10.5% compared to that of the reference Sn–Bi alloy, which can be attributed to the reduction in Sn-rich segregation and to grain refinement [44]. In particular, the toughness of the Sn–58Bi–0.03CNT composite increased

by 48.9% compared to that of the unreinforced Sn–Bi solder alloy [44]. In addition, corresponding fracture surface comparison between the Sn–58Bi–0.03CNT composite and the monolithic Sn–58Bi alloy was performed to identify the influence of CNTs on the fracture behavior [44].

The effects of graphene nanosheets on the mechanical properties of the Sn–58Bi–0.7Zn solder joint were investigated [45]. Experimental results and finite element simulations showed that the best mechanical property improvement came from the 0.076 wt.% graphene nanosheet-doped Sn–58Bi–0.7Zn sample [45]. For the thermal aging samples, the UTS of the solder joint was also increased by 2.04% [45].

The mechanical properties (the stress expansion and strain distribution during a single lap shear test) of the Sn–Bi–graphene nanocomposite according to the weight ratio of graphene were simulated based on the theoretical calculations of the finite element method [46]. The strength of the joint was found to be mainly influenced by the shear stress; initial cracking was found to occur at the edge of the joint [46]. The shear modulus of the Sn–Bi–graphene nanocomposite was 192% greater than that of the pure Sn–Bi alloy, when the content of graphene increased to 1.0 wt.% [46]. Stress concentration was found to exist near the edge of the graphene, where initial failure may occur [46].

Graphene nanosheets were successfully incorporated at various percentages (0, 0.01, 0.03, 0.05, or 0.1 wt.%) into Sn–58Bi solder [19]. The tensile properties, wettability, corrosion resistance, microhardness, and creep behavior were subsequently improved [19]. Tensile and nanoindentation tests reveal that the composite solder with 0.1 wt.% graphene nanosheets leads to enhancements of about 14 and 38%, respectively [19]. With 0.01 wt.% graphene nanosheet addition, the elongation is 49% greater than that of the pure Sn–58Bi solder alloy [19]. The creep performance and the corrosion resistance are all enhanced by addition of graphene nanosheets [19]. The mechanism of enhancement of the graphene nanosheets of the performance of the composite solder alloy is also analyzed in this work [19]. Tensile tests reveal that the UTS of the solders rises gradually with graphene nanosheet addition; there is a 14% enhancement of tensile strength for the Sn–58Bi–0.1graphene nanosheet [19]. The huge enhancement of 49% in the elongation of Sn–58Bi–0.01graphene nanosheet and the establishment of a brittle to ductile fracture mode are induced by the strengthening effect of graphene nanosheets [19]. The wettability is improved with graphene nanosheet addition because the nanosheets lower the interfacial surface energy between the solder and the substrate [19]. Moreover, the corrosion resistance is distinctly enhanced in the Sn–58Bi–0.1graphene nanosheet, and this material retains a lower corrosion rate than that of Sn–58Bi [19]. The hardness and creep resistance leads to an obvious improvement due to the addition of graphene nanosheets [19]. The hardness is enhanced by 38%, when the addition of graphene nanosheets increases to 0.1 wt.% [19]. The enhancement of the creep behavior is further illustrated by the variation of the creep mechanism in the solder alloys [19]. Among the composite solders synthesized, the Sn–58Bi–0.1graphene nanosheet provides the best tensile strength and hardness with decreased ductility (**Table 4**) [19].

Compositions	Additives	Causes	Results	References
Sn–58Bi	0.05 wt.% Cu_6Sn_5 nanoparticles	Brittle IMC nanoparticles	Creep resistance	[36]
Sn–58Bi	76 nm Ag nanoparticles	Refinement and dispersion	Microhardness and shear strength	[38]
Sn–58Bi	Al_2O_3 nanoparticles	Reinforcement effect	Electromigration resistance, shear strength, and microhardness	[39]
Sn–58Bi/Cu and Sn–58Bi/Cu–2.29Zn joints	Alloying 2.29 wt.% Zn to Cu substrate	Suppression of Cu_3Sn formation, Kirkendall voids, and Bi segregation at the IMC/Cu interface	Adhesion strength	[40]
Sn–57.6Bi–0.4Ag	0.5 wt.% W nanoparticles	Refined microstructure	Electromigration resistance and microhardness	[41]
Sn–58Bi, Sn–58Bi–0.5In, and Sn–58Bi–0.5Ni	0.5 wt.% In or Ni	Ni_3Sn_4 IMC formation at the grain boundaries	Shear strength degradation of Sn–58Bi–0.5Ni and improvement of Sn–58Bi–0.5In	[15]
Sn–58Bi	0.05, 0.1, 0.5, or 1.0 wt.% Ni	Ni_3Sn_4 IMC formation	Wetting behavior	[29]
Sn–58Bi/Cu joint	2.5 wt.% In addition to the solder	Cu–Sn–In IMCs	Wetting behavior	[13]
Sn–58Bi	0.0 or 0.7 wt.% Zn addition to the solder	Liquid-state aging	Ultimate tensile strength	[33]
Sn–58Bi/Cu joint	Sb addition	Increasing size of the grain	Wetting behavior	[18]
Sn–58Bi	2 wt.% In, 2 wt.% Ag, or each 2 wt.% In and Ag	$SnIn_{19}$ and Ag_3Sn IMCs (grain refiner)	Creep resistance	[42]
Sn–57.6Bi–0.4Ag	0.05 wt.% CNTs or Ni–CNTs	Ni_3Sn_4 IMCs	UTS and elongation	[43]
Sn–58Bi	0.03 wt.% MWCNTs	Reduction of Sn-rich segregation and refinement	Bending strength	[44]
Sn–58Bi–0.7Ag	Graphene nanosheets	Finite element simulation	UTS	[45]
Sn–58Bi	Graphene	Finite element method	Shear modulus	[46]
Sn–58Bi	0, 0.01, 0.03, 0.05, or 0.1 wt.% graphene nanosheets	Reinforcement effect	Tensile strength, wettability, corrosion resistance, hardness, and creep behavior	[19]

Table 4. The improvement of various mechanical properties of the low melting temperature solders.

4. Strategies for enhancing the electrical and thermo-mechanical performance of low melting temperature solder materials

The electrical and thermo-mechanical properties of many different low melting point solders are affected by a variety of processing factors, such as the reflow temperature, time, flux used and its effectiveness, and temperature of measurement [15, 36, 37, 40, 41, 45]. Furthermore, the change of chemical composition of solders according to the addition of supplementary additives is also considered as a main factor that modifies or even improves a solder's electrical and thermo-mechanical properties [15, 36, 37, 40, 41, 45]. Three main methods are used to improve the electrical and thermomechanical performance of low melting point solders: (i) doping with a small amount of certain elements via diffusion reactions, (ii) alloying with a large amount of certain elements, and (iii) reinforcing with metal or ceramic elements. Sometimes, (iv) all of these methods are combined for the enhancement of the intended properties of low melting temperature solders.

Transient liquid phase bonding was conducted using the Sn–Bi solder with 30 wt.% Cu particles added [37]. However, this process caused the melting point of the solder joints to increase from 139 to 201°C; In addition, the solder joints contained large voids, resulting in a considerable degradation in shear strength [37].

On a Cu substrate, the conventional Sn–58Bi solder was alloyed with 0.7 wt.% Zn to improve the interfacial reaction, tensile strength, and creep resistance during liquid-state aging [37]. However, the overgrown IMC layers between the Sn–58Bi solders and Cu substrates significantly degraded the reliability of the electronic products [37].

Lin et al. added minor amounts of Ga, ranging from 0.25 to 3.0 wt.% to Sn–58Bi solder [14]. As a result, the growth of IMC layers was effectively suppressed [14].

Hu et al. fabricated an Sn–58Bi composite solder reinforced with Al_2O_3 nanoparticles to slow down electromigration and to improve the shear strength and microhardness [39].

Four different concentrations of Ni (0.05, 0.1, 0.5, and 1.0 wt.%) were individually added to the Sn–58Bi solder [29]. The optimal concentration of Ni necessary to enhance the tensile strength of the alloy was 0.1 wt.%, but the elongation of the alloy was inversely correlated to the Ni content [29].

Wojewoda-Budka and a coworker demonstrated excellent diffusion soldering process results for Bi–22 at.% In on Cu interconnections; this was proved by the presence of $Cu_{11}In_9$ phase present in the Cu/In–22Bi/Cu interfaces in the temperature range of 85–200°C [47].

Graphene nanosheets were successfully incorporated at various percentages (0, 0.01, 0.03, 0.05, and 0.10 wt.%) into Sn–58Bi solder; the microstructure, tensile properties, wettability, corrosion resistance, hardness, and creep behavior were significantly improved [19].

Sun et al. introduced a low melting temperature Sn–57.6Bi–0.4Ag solder reinforced with different concentrations of MWCNTs or Ni-coated MWCNTs [35]. With the addition of

MWCNTs and Ni–MWCNTs, the fractured surface of the solder joints became rougher, leading to a better bonding structure [35]. Though both MWCNTs and Ni–MWCNTs have the capability to improve the mechanical performance of solder joints, Ni–MWCNTs worked much better [35]. The Ni coating was proved to significantly inhibit the aggregation of MWCNTs, which can solve cracks and wetting problems and even improve the strength of solder joints [35].

5. Concluding remarks

A recent trend in solder research mentioned that low melting temperature solder materials and their nanocomposite materials will be suitable for flexible interconnection applications in the near future. Thus, fabrications and/or syntheses, as well as elaboration of the electrical and thermomechanical properties, of various low melting temperature solder materials are discussed in detail. The various determination factors regarding the electrical and thermomechanical properties of solder materials are also elucidated with theoretical and experimental support. Subsequently, a promising approach to enhancing the performance of solder materials using supplementary additives, such as nanostructures, nanocomposites, alloying, and doping, is described with examples. It is possible to conclude that low melting temperature solders may enable significant advancement in interconnecting components in various applications and soldering technologies for the flexible microelectronic packaging industry.

Acknowledgements

This study was supported financially by Fundamental Research Program of the Korea Institute of Materials Science (KIMS). This work was also supported by the National Research Council of Science & Technology (NST) grant by the Korea government (MSIP) (No. CAP-12-6-KIMS).

Conflict of interest

With regard to competing financial interests, the authors declare that they have none.

Author details

Sang Hoon Kim and Sangsun Yang*

*Address all correspondence to: nanoyang@kims.re.kr

Powder Technology Department, Korea Institute of Materials Science, Changwon, Republic of Korea

References

[1] Gates BD. Materials science. Flexible electronics. Science. 2009;**323**:1566-1567

[2] Ko Y, Kim M, Bang J, Kim T, Lee C. Properties and reliability of solder microbump joints between Si chips and a flexible substrate. Journal of Electronic Materials. 2015;**44**:2458

[3] Kim SH, Son MJ, Nguyen VL, Lim T, Yang D, Kim M, Kim KB, Kim YJ, Lee JH, Kim YD. Preparation of property-controlled bi-based solder powders by a ball-milling process. Metals. 2016;**6**:74-84

[4] Kim SH, Yang D, Kim Y, Min T, Choi J, Yun J, Kim KB, Kim YJ, Lee JH, Do Kim Y. Thermomechanical evolution of ternary Bi–Sn–In solder micropowders and nanoparticles reflowed on a flexible PET substrate. Applied Surface Science. 2017;**415**:28-34

[5] Liu Y, Fu H, Sun F, Zhang H, Kong X, Xin T. Microstructure and mechanical properties of as-reflowed Sn–58Bi composite solder pastes. Journal of Materials Processing Technology. 2016;**238**:290-296

[6] Zardetto V, Brown TM, Reale A, Di Carlo A. Substrates for flexible electronics: A practical investigation on the electrical, film flexibility, optical, temperature, and solvent resistance properties. Journal of Polymer Science Part B: Polymer Physics. 2011;**49**:638-648

[7] Ho C, Lee P, Chen C, Yang C. Electromigration in 3D-IC scale Cu/Sn/Cu solder joints. Journal of Alloys and Compounds. 2016;**676**:361-368

[8] Frongia F, Pilloni M, Scano A, Ardu A, Cannas C, Musinu A, Borzone G, Delsante S, Novakovic R, Ennas G. Synthesis and melting behaviour of Bi, Sn and Sn–Bi nanostructured alloy. Journal of Alloys and Compounds. 2015;**623**:7-14

[9] Shu Y, Rajathurai K, Gao F, Cui Q, Gu Z. Synthesis and thermal properties of low melting temperature tin/indium (Sn/In) lead-free nanosolders and their melting behavior in a vapor flux. Journal of Alloys and Compounds. 2015;**626**:391-400

[10] Chen S, Chen C, Luo Z, Chao C. Fabrication and characterization of eutectic bismuth–tin (Bi–Sn) nanowires. Materials Letters. 2009;**63**:1165-1168

[11] Peng Y, Deng K. Fabrication of reduced graphene oxide nanosheets reinforced Sn–Bi nanocomposites by electro-chemical deposition. Composites Part A: Applied Science and Manufacturing. 2015;**73**:55-62

[12] Chang S, Wu S. Low-frequency damping properties of eutectic Sn–Bi and In–Sn solders. Scripta Materialia. 2011;**64**:757-760

[13] Chen X, Xue F, Zhou J, Yao Y. Effect of In on microstructure, thermodynamic characteristic and mechanical properties of Sn–Bi based lead-free solder. Journal of Alloys and Compounds. 2015;**633**:377-383

[14] Lin S, Nguyen TL, Wu S, Wang Y. Effective suppression of interfacial intermetallic compound growth between Sn–58wt.% Bi solders and Cu substrates by minor Ga addition. Journal of Alloys and Compounds. 2014;**586**:319-327

[15] Mokhtari O, Nishikawa H. Correlation between microstructure and mechanical properties of Sn–Bi–X solders. Materials Science and Engineering A. 2016;**651**:831-839

[16] Chriašteľová J, Ožvold M. Properties of solders with low melting point. Journal of Alloys and Compounds. 2008;**457**:323-328

[17] Shen J, Pu Y, Yin H, Luo D, Chen J. Effects of minor Cu and Zn additions on the thermal, microstructure and tensile properties of Sn–Bi-based solder alloys. Journal of Alloys and Compounds. 2014;**614**:63-70

[18] Zhang C, Liu S, Qian G, Jian Z, Feng X. Effect of Sb content on properties of Sn–Bi solders. Transactions of Nonferrous Metals Society of China. 2014;**24**:184-191

[19] Ma Y, Li X, Zhou W, Yang L, Wu P. Reinforcement of graphene nanosheets on the microstructure and properties of Sn58Bi lead-free solder. Materials and Design. 2017;**113**:264-272

[20] Yan L, Lee C, Yu D, Yu A, Choi W, Lau J, Yoon S. A hermetic seal using composite thin-film In/Sn solder as an intermediate layer and its interdiffusion reaction with Cu. Journal of Electronic Materials. 2009;**38**:200-207

[21] Chen S, Lee W, Hsu C, Yang C, Hsu H, Wu H. Sn–In–Ag phase equilibria and Sn–In–(Ag)/Ag interfacial reactions. Materials Chemistry and Physics. 2011;**128**:357-364

[22] Li J, Mannan S, Clode M, Whalley D, Hutt D. Interfacial reactions between molten Sn–Bi–X solders and cu substrates for liquid solder interconnects. Acta Materialia. 2006;**54**:2907-2922

[23] Islam M, Chan Y, Rizvi M, Jillek W. Investigations of interfacial reactions of Sn–Zn based and Sn–Ag–Cu lead-free solder alloys as replacement for Sn–Pb solder. Journal of Alloys and Compounds. 2005;**400**:136-144

[24] Tian F, Liu Z, Shang P, Guo J. Phase identification on the intermetallic compound formed between eutectic Sn–In solder and single crystalline Cu substrate. Journal of Alloys and Compounds. 2014;**591**:351-355

[25] Li MY, Yang HF, Zhang ZH, Gu JH, Yang SH. Fast formation and growth of high-density Sn whiskers in Mg/Sn-based solder/Mg joints by ultrasonic-assisted soldering: Phenomena, mechanism and prevention. Scientific Reports. 2016;**6**:27522

[26] Zhao N, Zhong Y, Huang ML, Ma HT, Dong W. Growth kinetics of Cu_6Sn_5 intermetallic compound at liquid-solid interfaces in Cu/Sn/Cu interconnects under temperature gradient. Scientific Reports. 2015;**5**:13491

[27] Huang M, Yang F. Size effect model on kinetics of interfacial reaction between Sn–xAg–yCu solders and Cu substrate. Scientific Reports. 2014;**4**:7117

[28] Kumar KM, Kripesh V, Tay AA. Single-wall carbon nanotube (SWCNT) functionalized Sn–Ag–Cu lead-free composite solders. Journal of Alloys and Compounds. 2008;**450**:229-237

[29] Kanlayasiri K, Ariga T. Physical properties of Sn–58Bi–xNi lead-free solder and its interfacial reaction with copper substrate. Materials and Design. 2015;**86**:371-378

[30] Mu W, Zhou W, Li B, Wu P. Janus-faced Cu-core periphery formation and Bi phase redistribution under current stressing in Cu-cored Sn–58Bi solder joints. Journal of Alloys and Compounds. 2014;**584**:483-486

[31] Altıntas Y, Kaygısız Y, Öztürk E, Aksöz S, Keşlioğlu K, Maraşlı N. The measurements of electrical and thermal conductivity variations with temperature and phonon component of the thermal conductivity in Sn–Cd–Sb, Sn–In–Cu, Sn–Ag–Bi and Sn–Bi–Zn alloys. International Journal of Thermal Sciences. 2016;**100**:1-9

[32] Zhang S, Chen Q. Fabrication of MWCNT incorporated Sn–Bi composite. Composites Part B: Engineering. 2014;**58**:275-278

[33] Ping W. Effects of Zn addition on mechanical properties of eutectic Sn–58Bi solder during liquid-state aging. Transactions of Nonferrous Metals Society of China. 2015;**25**:1225-1233

[34] Aksöz S, Maraşlı N, Keşlioğlu K, Yıldız F. Variations of thermal conductivity with temperature and composition of Zn in the Bi–[x] at.% Zn–2 at.% Al alloys. Thermochimica Acta. 2012;**547**:1-5

[35] Sun H, Chan Y, Wu F. Effect of CNTs and Ni coated CNTs on the mechanical performance of Sn57.6Bi0.4Ag BGA solder joints. Materials Science and Engineering A. 2016;**656**:249-255

[36] Li X, Ma Y, Zhou W, Wu P. Effects of nanoscale Cu_6Sn_5 particles addition on microstructure and properties of Sn–Bi solder alloys. Materials Science and Engineering A. 2017;**684**:328-334

[37] Mokhtari O, Nishikawa H. The shear strength of transient liquid phase bonded Sn–Bi solder joint with added Cu particles. Advanced Powder Technology. 2016;**27**:1000-1005

[38] Li Y, Chan Y. Effect of silver (Ag) nanoparticle size on the microstructure and mechanical properties of Sn–58Bi–Ag composite solders. Journal of Alloys and Compounds. 2015;**645**:566-576

[39] Hu T, Li Y, Chan Y, Wu F. Effect of nano Al_2O_3 particles doping on electromigration and mechanical properties of Sn–58Bi solder joints. Microelectronics Reliability. 2015;**55**:1226-1233

[40] Wang F, Zhou L, Wang X, He P. Microstructural evolution and joint strength of Sn–58Bi/Cu joints through minor Zn alloying substrate during isothermal aging. Journal of Alloys and Compounds. 2016;**688**:639-648

[41] Li Y, Luo K, Lim AB, Chen Z, Wu F, Chan Y. Improving the mechanical performance of Sn57.6Bi0.4Ag solder joints on Au/Ni/Cu pads during aging and electromigration through the addition of tungsten (W) nanoparticle reinforcement. Materials Science and Engineering A. 2016;**669**:291-303

[42] Shalaby RM. Effect of silver and indium addition on mechanical properties and indentation creep behavior of rapidly solidified Bi–Sn based lead-free solder alloys. Materials Science and Engineering A. 2013;**560**:86-95

[43] Yang L, Zhou W, Liang Y, Cui W, Wu P. Improved microstructure and mechanical properties for Sn–58Bi solder alloy by addition of Ni-coated carbon nanotubes. Materials Science and Engineering A. 2015;**642**:7-15

[44] Peng H, LÜ X, Lin T, LI H, Jing A, Xin M, FENG J, Zhang Y, Qi L, QIAN Y. Improvement of mechanical properties of Sn–58Bi alloy with multi-walled carbon nanotubes. Transactions of Nonferrous Metals Society of China. 2012;**22**:s692-s696

[45] Ma D, Wu P. Effects of coupled stressing and solid-state aging on the mechanical properties of graphene nanosheets reinforced Sn–58Bi–0.7Zn solder joint. Materials Science and Engineering A. 2016;**651**:499-506

[46] Peng Y, Deng K. Study on the mechanical properties of the novel Sn–Bi/Graphene nanocomposite by finite element simulation. Journal of Alloys and Compounds. 2015;**625**:44-51

[47] Wojewoda-Budka J, Zięba P. Formation and growth of intermetallic phases in diffusion soldered Cu/In–Bi/Cu interconnections. Journal of Alloys and Compounds. 2009;**476**:164-171